

Geo-Congress 2026

GSP 381

Geosynthetics, Pavements, and Soil Improvement

Selected Papers from Geo-Congress 2026
Salt Lake City, Utah | March 9–12, 2026

Edited by

Jack Montgomery, Ph.D., P.E.
Brady R. Cox, Ph.D., P.E.

ASCE

G-I GEO-INSTITUTE ASCE

GEOTECHNICAL SPECIAL PUBLICATION NO. 381

GEO-CONGRESS 2026

GEOSYNTHETICS, PAVEMENTS, AND SOIL IMPROVEMENT

SELECTED PAPERS FROM SESSIONS OF GEO-CONGRESS 2026

March 9–12, 2026
Salt Lake City, Utah

SPONSORED BY

The Geo-Institute
of the American Society of Civil Engineers

EDITED BY
Jack Montgomery, Ph.D., P.E.
Brady R. Cox, Ph.D., P.E.

Published by the American Society of Civil Engineers

Published by American Society of Civil Engineers
1801 Alexander Bell Drive
Reston, Virginia, 20191-4382
www.asce.org/publications | ascelibrary.org

Any statements expressed in these materials are those of the individual authors and do not necessarily represent the views of ASCE, which takes no responsibility for any statement made herein. No reference made in this publication to any specific method, product, process, or service constitutes or implies an endorsement, recommendation, or warranty thereof by ASCE. The materials are for general information only and do not represent a standard of ASCE, nor are they intended as a reference in purchase specifications, contracts, regulations, statutes, or any other legal document. ASCE makes no representation or warranty of any kind, whether express or implied, concerning the accuracy, completeness, suitability, or utility of any information, apparatus, product, or process discussed in this publication, and assumes no liability therefor. The information contained in these materials should not be used without first securing competent advice with respect to its suitability for any general or specific application. Anyone utilizing such information assumes all liability arising from such use, including but not limited to infringement of any patent or patents.

ASCE and American Society of Civil Engineers—Registered in U.S. Patent and Trademark Office.

Photocopies and permissions. Permission to photocopy or reproduce material from ASCE publications can be requested by sending an e-mail to permissions@asce.org or by locating a title in ASCE's Civil Engineering Database (http://cedb.asce.org) or ASCE Library (http://ascelibrary.org) and using the "Permissions" link.

Errata: **Errata, if any, can be found at https://doi.org/10.1061/9780784486764**

Copyright © 2026 by the American Society of Civil Engineers.
All Rights Reserved.
ISBN 978-0-7844-8676-4 (PDF)
Manufactured in the United States of America.

Preface

This is the seventh volume of seven Geotechnical Special Publications (GSPs) containing papers from Geo-Congress 2026: Geo Tools, Technologies, and Techniques in an Environment of Change, held in Salt Lake City, Utah, on March 9-12, 2026. Notably, this conference marks the 30th anniversary of the Geo-Institute. The conference brought together industry leaders, researchers, and practitioners to showcase innovations, address critical challenges, and advance knowledge in geotechnical engineering. The conference hosted the Terzaghi, Peck, Seed, and Prakash Lectures and many technical sessions, panel sessions, short courses, and student competitions.

These proceedings represent the culmination of nearly two years of effort by the program committee and many other individuals, whose focus has been to continue the success of previous Geo-Congresses and to celebrate 30 years of geotechnical innovation by the Geo-Institute. Building the program started with an international call for papers that resulted in more than 800 abstracts on a variety of important topics. Each paper was subjected to a rigorous technical review by two or more independent peer reviewers. Acceptance required concurrence by at least two peer reviewers, and final decisions were made only after review coordinators confirmed that authors satisfactorily addressed any reviewer comments on their original submission. All accepted papers are presented at the conference as posters or technical talks and are eligible for applicable ASCE awards.

This volume contains a collection of 60 papers focused primarily on the topics of geosynthetics, pavements, and soil improvement. This includes papers on innovative materials and ground improvement techniques, pavement geotechnics, and design and performance of various types of geosynthetics.

The success of this conference and proceedings would not have been possible without the participation and collaboration of many individuals, including Brad Keelor, the tireless staff at the Geo-Institute, and the many session chairs and reviewers. We hope that these proceedings will be of use to the geotechnical engineering community for many years to come.

The Editors,

Jack Montgomery, Ph.D., P.E., M.ASCE, Auburn University
Brady R. Cox, Ph.D., P.E., M.ASCE, Utah State University

© ASCE

Acknowledgments

We are very grateful for the contributions of the authors, peer reviewers, session chairs, and program committee, without whom this publication would not be possible.

Geo-Congress 2026 Conference Program Committee

Conference Chairs
K. N. Gunalan, Ph.D., P.E., BC.GE, Pres. 20 ASCE, NAC, HNTB Corporation
Ryan B. Maw, P.E., G.E., BC.GE, F.ASCE, Gerhart Cole

Technical Chair
Shideh Dashti, Ph.D., M.ASCE, University of Colorado Boulder

Proceedings Editors
Brady R. Cox, Ph.D., P.E., M.ASCE, Utah State University
Jack Montgomery, Ph.D., P.E., M.ASCE, Auburn University

Student Program Liaison
Cassandra Rutherford, Ph.D., P.E., M.ASCE, Iowa State University

Program Committee Members
Aaron L. Leopold, P.E., M.ASCE, Dan Brown and Associates
Kam Ng, Ph.D., P.E., M.ASCE, University of Wyoming
Jenny Ramirez, Ph.D., P.E., M.ASCE, Geosyntec Consultants

© ASCE

Contents

Geosynthetics

A Laboratory Protocol for Simulating Installation Damage in PVC-Coated PET Woven Geogrids Based on a Targeted Reduction Factor.....1
Sezgin Sarak, Burak Tanyu, and Erol Guler

Comparative Study of Wicking and Conventional Geotextiles: Interface Properties and Drainage Performance for Slope Reinforcement.....10
Jaime Suarez, Puneet Bhaskar, Darlene Goehl, and Anand J. Puppala

Design and Performance Evaluation of Geosynthetic-Reinforced Load Transfer Platforms in Pile-Supported Embankments.....20
Masoud Nobahar and Murad Y. Abu-Farsakh

Effect of Linear Polymer on Water Retention Behavior of Bentonite-Polymer Geosynthetic Clay Liner.....30
Hanrui Zhao, Benjamin M. Stark, and Kuo Tian

Evaluating Pavement Resilience to Freeze-Thaw Cycles Using Geocell and Geocomposite Reinforcements: A Two-Year Field Study 38
Berjees Anisa Ikra, Yongxuan Gao, Jiming Liu, Taylor Dagenais, Arghya Chatterjee, Sanat Pokharel, Min Sun, and Cheng Lin

Geogrid Stabilization of Railway Ballast under Varying Moisture Conditions Evaluated Using Bender Element Shear Wave Technology 48
Youngdae Kim, Hyunsoo Lee, Han Wang, Erol Tutumluer, Hugh Thompson, and Theodore R. Sussmann

Investigating the Impact of Cold Weather Aging and Temperature on Rock Simulant Puncture Resistance of Geomembranes 58
Calvin Tohm, Isaac Nedved, and Bret N. Lingwall

Multi-Axial In-Plane Creep Testing of Geogrids.....68
Emre Duman, Michael Bauby, and J. David Frost

New Nanocoating for EPS Blocks: Testing, Modeling, and Cost 78
Sherif S. AbdelSalam, Mohamed M. Omran, Moamen A. Shekib, Ahmed M. Ahmed, and Emad S. Bakhoum

Performance Evaluation of Geosynthetic-Reinforced Subgrade Soils Using Dynamic Cone Penetrometer Testing.....93
Laith Ibdah, Kenaz Owusu, Ali Behdad, Yan Feng, and Jongwan Eun

© ASCE

Performance of Glass-Based Geosynthetic Reinforced RAP Bases for Unpaved Road Applications 103
Krishneswar Ramineni, Shanmukha Sai Avinash Gonnabathula, Jianxin Huang, Puneet Bhaskar, Balaji Lakkimsetti, and Anand J. Puppala

Performance of Strip Foundations Reinforced with 3D-Printed Geocells 113
Sarper Demirdogen and Ayhan Gurbuz

Quantifying Geogrid-Stabilized Aggregate Response in Dynamic Loading Environments 124
Syed Faizan Husain and Erol Tutumluer

Pavements

Appraising the Potential to Responsibly Recycle Plastic within Pavements, Pipe, and Rail Infrastructure 134
Jason Stewart, Abby Cisko, Chris Wacinski, and Isaac L. Howard

Characterization of Foamed Asphalt Stabilized Base Course Layers for the Thickness Design of Airport Pavements 145
Greg White

Enhancing Granular Surface Material Performance Using California Bearing Ratio and Repeated Load Triaxial Tests 155
Mahsa Belalzadeh, Jeramy Ashlock, Umar Farooq, and Bora Cetin

Numerical Analysis of Climate-Induced Changes in Pavement Subgrade Performance 167
Amanda Sampaio and Yuderka Trinidad González

Optimization of Metakaolin-Cement Proportions for Stabilizing Aggregate Quarry Byproducts: Mechanical Property Assessment 177
Taeyun Kong, Issam I. A. Qamhia, and Erol Tutumluer

Performance of Wicking Geotextile for Flexible Pavements Built over Frost Susceptible Soils 186
Md. Fyaz Sadiq, Danial Mirzaiyan, Mohammad Wasif Naqvi, Bora Cetin, and Raul Velasquez

Quality of Recycled Materials Resulting from Full-Depth Reclamation of an Airfield Asphalt Pavement 198
Victor M. Garcia, Mark Different, Alvaro Rodriguez, and Waldemar Perez

Verification of a Finite Element Model Utilized to Simulate the Vibratory Response of a Compaction Roller 209
William J. Baker III and Christopher L. Meehan

© ASCE

Soil Improvement

3D Numerical Study on Geosynthetically Reinforced Stone Columns 220
Hossein Bahmyari, Mohebollah Agahnav, Ali Noorzad,
and Mohammad Jammali Moghadam

A History of Foundation Engineering in Windsor, Ontario, and Developments in Prefabricated Vertical Drain Design 229
Mark Henderson

A Sustainable Hybrid Stabilization Approach for Expansive Soils: Integrating Enzyme-Induced Carbonate Precipitation with Sodium Alginate Biopolymer 240
Shantanu Paul, Anas Bin Faruque, Azmain Mottaqi, and Ojashwy Islam Audri

Aggressive Rehabilitation of Gravel Roads with and without Enzymatic Soil Stabilizers.....251
Godfred F. Akwaa and Jeramy Ashlock

Antifreeze Cellulose Nanofiber Gels for the Sustainable Improvement of Soils against Freeze-Thaw Deformations.....262
Mohammadhasan Sasar and Sherif L. Abdelaziz

Application of Coal-Derived Char in Cement-Stabilized Sodium Bentonite-Sand Soil for Subgrade Applications.....271
Kamal Gautam, Hua Yu, Chooi Kim Lau, and Kam Ng

Cement Enhanced Short Columns for Stabilizing Plastic Clays under Structures.....282
Muawia Dafalla and Abdullah A. Shaker

Compressible Soil Considerations for the Design and Construction of a Water Treatment Facility.....290
Stoney L. Mather, Bryan W. Franke, and Braden M. Error

Consolidation Behaviour of Stone Column-Improved Soft Soil under Different Applied Stress Conditions.....306
T. S. D. Venkatesh, Kousik Deb, and Aniruddha Sengupta

Development of Erosion Functions for Florida Beach Sand Treated with Bioslurry 317
Saeed Booshi, Peter Schmillen, Amar Kosovac, Raphael Crowley,
Terri N. Ellis, and Brian Wingender

Durability of Zein-Treated Sand under Wetting-Drying Cycles.....327
Quadri Olakunle Babatunde, Adolf Yaw Minta, Yoon Geom Heo,
and Yong-Hoon Byun

© ASCE

Effect of Clay Mineralogy on the Extent of Ettringite-Induced Heaving in Lime-Treated Sulfate-Rich Soils **333**
Ajeyo Mukherjee, Vipul Kotha, Sayantan Chakraborty, Suresh S, Nripojyoti Biswas, and Suman Roy

Effects of MICP Stabilization Using Aerobic Denitrification and Non-Sterile Ureolysis Pathways on Sand Column Properties **344**
Yasaman Abdolvand and Mohammadhossein Sadeghiamirshahidi

Engineering Performances of Silty Sand Stabilized by Reactive Magnesia Activated Granulated Blast-Furnace Slag **354**
Qianwei Ma, Bowen Yu, and Ningjun Jiang

Enhancing Durability and Permanency of Problematic Soils Using Silica-Based Co-Additives with Calcium-Based Stabilizers **364**
Nripojyoti Biswas, Sopharith Chou, Krishneswar Ramineni, Sayantan Chakraborty, and Anand J. Puppala

Enhancing Shear Strength of Sandy Soils Using Enzyme-Induced Carbonate Precipitation and Sodium Alginate Biopolymer **375**
Shantanu Paul, Anas Bin Faruque, Azmain Mottaqi, and Arzida Binta Anwar

Enhancing the Performance of Biopolymer Stabilization of Sulfate-Rich Expansive Soil Using Co-Additives **385**
Debayan Ghosh and Aritra Banerjee

Evaluating Chemically Stabilized Soils Using Geochemical Pore Solution Modeling **394**
Ashish Bastola, Pavan Akula, and John F. Rushing

Evaluating the Effect of MICP Treatment on Problematic Calcareous Soil of Hormoz Island in Iran **404**
Yasaman Abdolvand, Mohammadhossein Sadeghiamirshahidi, and Mohammad Vahid

Evaluation of the Bearing Capacity of Ring Foundations Placed on Weak Clays Reinforced with Circular and Annular Stone Columns **415**
Sudipto Mukherjee

Experimental Study of the Mechanical and Durability Properties of a Collapsible Soil Treated with Biopolymers **425**
Shamontee Aziz, Pushan Bal, Scott M. Olson, and Paul V. Braun

Feasibility Study of Quantifying the Soil Strength Improvement from Polyurethane Injection **436**
Chadi El Mohtar, Kowshik Kumar, Bianca Zuleta, and Abhilash Reddy

© ASCE

Fluidization and Stabilization of Soft Soil Subgrades under Cyclic Rail Loading.....447
Buddhima Indraratna, Bin-Hua Xu, Cholachat Rujikiatkamjorn, Joseph Arivalagan, and Mandeep Singh

Ground Improvement for Liquefaction Mitigation at Sevier Bridge Dam.....457
Travis Gerber, Jed McFarlane, Ryan Cole, Richard Buhler, and Phil Gerhart

Impact of Hydrophobic Material on Kaolin Slurry Consolidation.....469
Kushal Sharma, Ruoyu Zheng, Xinbao Yu, and Laureano Hoyos

Improvement of Mechanical Properties and Erosion Resistance in Soils Using Biopolymers for Sustainable Geotechnical Applications.....478
Bin Zhang and Kejun Wen

Improving Strength and Cohesion in 3D-Printed Soil Composites Using Xanthan Gum.....488
Sampson J. Arku and Cassandra J. Rutherford

Influence of Cement Dosage and Plasticity on the Stiffness of Stabilised Clays: Classification and Mechanical Response.....496
Balaji Bandaru, R. G. Robinson, and Ramesh Kannan Kandasami

Innovative Electrokinetic Treatment of Expansive Soils: Evaluating $MgCl_2$ and $CaCl_2$ as Stabilizing Agents.....502
Najibullah Zulfeqar, Shiqiang Zou, and Ali Khosravi

Laboratory Study on Stiffness and Strength of Cement Stabilized Clay Subjected to Four-Season Durability Cycles.....512
Kyle Parr, Jianxin Huang, Anand J. Puppala, and Jeb S. Tingle

Lab-Scale Evaluation of Using Type IL and LC3 Cements in Deep Mixing Applications: Stage One—Fresh Grout Properties.....521
Mahsa Salehi Nia and Chadi El Mohtar

Nonlinear Simulation of the Seismic Performance of Unreinforced and Fiber-Reinforced Rigid Inclusions in Soft Soil Site.....532
Daniel Hutabarat, James Gingery, and Francisco Humire

Optimized Foundation Design and Construction for Provo, UT, Wastewater Treatment Plant.....543
Lisheng Shao, Aaron Leopold, Mathew Francis, Tim Siegel, Mike Robison, Scott Simmons, Rob Jameson, and Scott Chambers

Performance Assessment of Self-Induced and Externally Induced Pozzolanic Reactions in Lime-Treated Expansive Soil.....555
S. Chandru and S. Jayalekshmi

© ASCE

Quality Assurance and Quality Control in the Installation of Lightweight Cellular Concrete **565**
Trevor Towery, Ryan Maw, and Zach Gibbs

Rethinking the Role of Downdrag in Rigid Inclusion Design **575**
Sonia S. Swift, Kevin R. Johnson, and Mary C. Nodine

Static and Cyclic Behavior of Oil Contaminated Sand **587**
Anjali Verma and Nihar Ranjan Patra

Use of Recycled Rubber Granulates in Railway Subballast for Improved Track Performance **598**
Yujie Qi, Buddhima Indraratna, and Rakesh Malisetty

Utilizing Lime Sludge as a Co-Additive to Cement Stabilized Expansive Soils under Cyclic Environmental Stressors **609**
Sopharith Chou, Jianxin Huang, Anand J. Puppala, Bora Cetin, and Raul Velasquez

© ASCE

A Laboratory Protocol for Simulating Installation Damage in PVC-Coated PET Woven Geogrids Based on a Targeted Reduction Factor

Sezgin Sarak[1]; Burak Tanyu, Ph.D.[2]; and Erol Guler, Ph.D.[3]

[1]Ph.D. Candidate, Dept. of Civil, Environmental, and Infrastructure Engineering, George Mason Univ., Fairfax, VA. Email: ssarak@gmu.edu
[2]Dept. of Civil, Environmental, and Infrastructure Engineering, George Mason Univ., Fairfax, VA. Email: btanyu@gmu.edu
[3]Dept. of Civil, Environmental, and Infrastructure Engineering, George Mason Univ., Fairfax, VA. Email: fguler@gmu.edu

ABSTRACT

During the construction of geogrid-reinforced earth structures, geogrids are often subjected to compaction-induced damage, which may reduce their tensile strength. This potential loss is typically addressed by applying a reduction factor to the tensile strength for installation damage (RFID). The RFID values can be determined from the existing standard protocols by testing a specific geogrid. This approach works well for design purposes, but if the intention is to produce damaged geogrid specimens for further investigation, where the damage is associated with specific RFID values, the existing standard protocols fall short. The focus of this study is to close this gap by presenting an approach on how to create uniform damage distribution on the geogrid surface that corresponds to a specific RFID value. The procedure was developed using a polyvinyl chloride (PVC) coated polyester (PET) woven geogrid because of the wide usage of this type of geogrid as reinforcement. Based on the literature, two target RFID values were selected for this study. For consistency with existing standard protocols, the geogrid was compacted between aggregate layers. Damage was created by changing the compaction energy and the thickness of the aggregate layer above the geogrid. The uniformity of damage was confirmed through image analysis and the magnitude of strength loss using single-rib tensile tests. The tensile strength test results were also used to confirm target RFID values.

INTRODUCTION

Geosynthetic-reinforced mechanically stabilized earth (GMSE) walls have been widely used in the United States since the 1970s (Allen et al. 2001, El-Sherbiny and Gross 2009). Typical construction process for GMSE wall involves placement of the geosynthetic reinforcement in between compacted backfill layers and connecting the geosynthetic to the wall face either by frictional or mechanical interlocking systems (Han et al. 2018). The term installation damage typically focuses on the interaction between the geosynthetic and the backfill layers and does not include the part that is associated with the wall face connections. The damage on geosynthetic may occur due to various mechanisms such as tearing, excessive tensile strain, abrasion from dynamic and static loads during compaction, and filament breakage (Lim and McCartney 2013).

Accurate quantification of installation damage and accounting for this damage in design calculations are important to assess the long-term performance of the installed geosynthetics. Numerous field studies have shown that installation damage is a function of the geosynthetic type (manufacturing method, polymer type, coating condition if applicable), aggregate properties

© ASCE

(grain size distribution, maximum particle size, and angularity), and compaction effort (vibration energy, lift thickness, and number of passes) (Koerner et al. 1993, Lopes et al. 2000, Hsieh and Wu 2001, Hufenus et al. 2005, Cho et al. 2006, Lim and McCartney 2013). Therefore, existing guidelines to implement full-scale field tests to assess damage to geosynthetics also account for GMSE wall components such as aggregate type, gradation of aggregate, and compaction effort (BSI 8006-1 2010, ASTM D5818 2022). The reduction factor due to installation damage (RFID) is determined by comparing the tensile strength of the geosynthetics before and after the geosynthetic is exposed to the installation conditions. As noted by Koerner and Koerner (2018), geogrids are the most common geosynthetic reinforcement type in GMSE walls, and the EN ISO 10722 (2019) standard outlines an index test procedure in which a geogrid specimen is subjected to repeated loading between two granular layers, with damage assessed through visual inspection and tensile strength loss. Since installation conditions vary across projects, guidelines recommend a range of RFID values for MSE wall design rather than a single number (Elias et al. 2001, Tanyu et al. 2008, Taylor et al. 2023).

The ranges of RFID values may be sufficient for design, but they do not provide a laboratory means to generate geogrid specimens with specific, predefined RFID values. In some cases, the intent is not only to select an RFID for design but to produce damaged geogrids for further investigation, such as mechanical or durability testing, where the specimens must reflect a consistent and targeted level of damage. No standardized laboratory protocol currently exists for this purpose. Previous studies mainly examined the influence of parameters such as aggregate size, lift thickness, or compaction effort without establishing a systematic approach for achieving specific target RFID values (Hufenus et al. 2005; Ching-Chuan and Shuay-Luen 2006; Huang and Wang 2007; Domiciano et al. 2020). The study presented in this manuscript addresses this gap by developing a laboratory protocol that simulates compaction-induced damage corresponding to targeted installation reduction factors. The protocol was deliberately designed to produce specimens with uniformly distributed damage, thereby minimizing variability and improving consistency in subsequent evaluations of damaged geogrids.

LABORATORY TEST SET-UP AND MATERIALS USED IN THIS STUDY

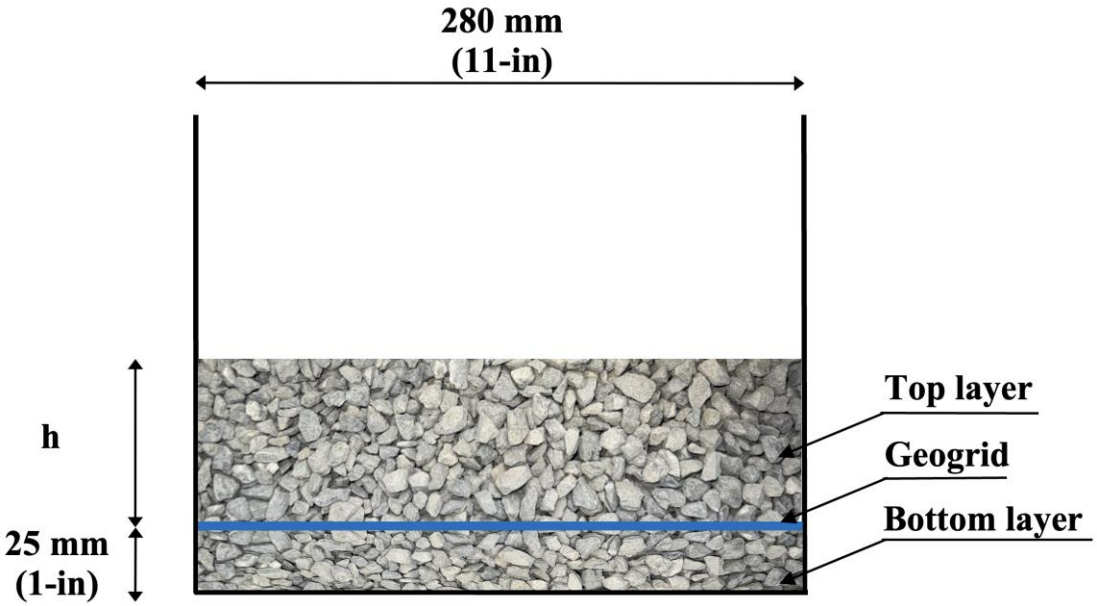
One of the most widely used geogrid for reinforcement application is identified in the literature as PVC-coated, polyester yarn woven geogrid (Shinoda and Bathurst 2004, Zornberg and Christopher 2007, El-Sherbiny and Gross 2009, Koerner and Koerner 2018). Therefore, this study focused on using this type of geogrid for the methodology presented in this paper. The properties of the geogrid is presented in Table 1.

The test set-up used in this study consisted of a cylindrical mold, aggregate, geogrid, and vibratory hammer. The geogrid was placed between the bottom and the top aggregate layers (Figure 1). The same material with the same gradation was used for both the bottom and top layers. The aggregate was produced from diabase rock crushed at a quarry in Northern Virginia. This type of aggregate is widely used in transportation infrastructure projects in Virginia. Based on the classification by Powers (1953), the aggregate particles exhibit low sphericity and range from angular to very angular (Figure 2). These shape characteristics were particularly favorable for inducing damage to the geogrid. The particle size was selected between 5 mm (0.2-in) and 10 mm (0.39-in) following the recommendations of EN ISO 10722 (2019) and Taylor et al. (2023). To achieve this range, the aggregate was sieved through a sieve with 9.5 mm (3/8-in) opening and the particles retained on the No. 4 sieve (4.75 mm opening) were used in this study.

© ASCE

Table 1. Manufacturer reported mechanical properties of the geogrid used in this study.

Mechanical Properties	Test Method	Unit	Minimum Average Roll Value
Tensile Strength @ Ultimate	ASTM D6637 (Method B)	lbs/ft (kN/m)	3650 (53.3)
Tensile Strength @ 5% Strain	ASTM D6637 (Method B)	lbs/ft (kN/m)	1250 (18.2)
Creep Rupture Strength	ASTM D5262/D6992	lbs/ft (kN/m)	2535 (35.5)



Note: h refers to the thickness of the top aggregate layer

Figure 1. Schematic of the test set-up used in this study.



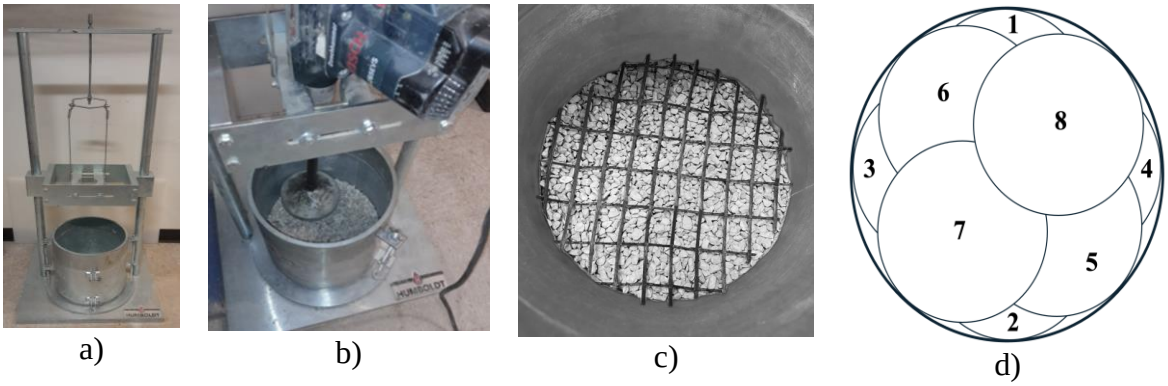
Figure 2. Photo of the aggregate particles used in this study.

The cylindrical mold used in this study has a diameter of 280 mm (11-in) and height of 305 mm (12-in) (Figure 3a). The mold dimensions and test set-up are consistent with ASTM D7382

© ASCE

(2020) for vibratory compaction tests. This facilitated the effective transfer of the applied loading from the hammer to the aggregate (Figure 3b). The hammer used for this application was a Bosch rotary hammer (model 3611 B64), capable of applying approximately 3200–3500 blows per minute, an impact energy of 9.5-12 m-N (7 and 9 ft-lbf). The geogrid was cut in a circular shape to match the mold's diameter (Figure 3c), producing a specimen large enough to yield eight single-rib tensile test samples. This configuration allowed consistent replication of tensile test results.

Given the maximum particle size of 9.5 mm, the bottom layer thickness was set to 25 mm (1-in) to provide sufficient space for particle movement during compaction. The maximum dry density of the aggregate, determined in accordance with ASTM D7382 (2020), was 15.8 kN/m^3 (100.5 lb/ft^3), and the aggregate was compacted to 100% relative compaction.



a) b) c) d)

Figure 3. The cylindrical mold (a) setup, (b) placement of the compaction hammer and (c) geogrid within the mold, and (d) the hammer patterns applied during tests

The pressure to cause damage to geogrid was applied to the top of the top layer (Figure 3b). The locations of the hammer to apply this pressure were selected to match the pattern described in ASTM D7382 (2020) (Figure 3d). Therefore, for each condition, the top aggregate was compacted from 8 different surface locations.

Tests were conducted based on two variables:

- changing the thickness of the top layer (h in Figure 1), and
- changing the duration of the applied vibratory compaction

These variables were iteratively changed until uniform damage across the geogrid surface was achieved and the tensile strength reduction corresponded to the target reduction factors that were aimed in this study. When adjusting the duration of the vibratory compaction of the top layer, the revised duration was uniformly applied to each of the predefined hammer locations shown in Figure 3d. Each test was conducted with virgin aggregate, no material was reused for any tests.

The range of RFID values to be considered in the design of PVC-coated PET yarn woven geogrids is suggested by the Federal Highway Administration (FHWA) for Type-2 backfill, which includes the grain size used in this study, is between 1.1 and 1.3 (Taylor et al., 2023). Ching-Chuan and Shuay-Luen (2006) for the same type of geogrid reported the RFID values to range between 1.00 and 1.16. In Ching-Chuan and Shuay-Luen (2006) study, the test set-up included a hydraulic cyclic loading system, where the load is applied from the top of aggregate. The RFID range was determined by changing the grain size distribution of the aggregate, lift

© ASCE

thicknesses, and compaction efforts. Even though Taylor et al. (2023) recommend RFID values to be as high as 1.3, as Ching-Chuan and Shuay-Luen demonstrated, it is possible that the range of RFID values for PVC coated PET geogrids could be much less than 1.3. Therefore, in this study, the target RFID values were chosen as 1.05 and 1.1. The 1.05 was chosen to represent modest damage and 1.1 to target the FHWA recommendation. Even though these RFID values were used in this study, the methodology followed herein may be revised to achieve other RFID values that may be an interest.

ASSESSMENT OF DAMAGE DISTRIBUTION ON THE GEOGRID SURFACE

Image analysis was employed to evaluate the distribution of installation damage on the geogrid surface. As a first step, virgin geogrid specimens were analyzed to establish a baseline reference for comparison with the damaged samples. Images of the undamaged specimens were captured under various lighting conditions and viewing angles to generate a standardized reference of the intact surface. To maintain consistent imaging geometry, the geogrid was positioned at a fixed location on a marked tabletop, and the camera was mounted at a constant height above the specimen. To account for lighting variability, images were collected under natural daylight, overhead fluorescent lighting, and indirect LED illumination. In addition, the table was rotated in 60° increments to complete a full 360° cycle, and images were taken at each step to capture reflections from different perspectives.

The polyester geogrid used in this study is coated with a black PVC layer, while the PET yarns appear light gray. In the image analysis, mechanical damage to the PVC coating was identified by visible color variations associated with material loss. These variations were quantified through grayscale intensity histograms. Baseline images of the virgin geogrids were then compared with those of the damaged specimens to detect changes after installation damage. It should be noted that the image analysis was not intended for quantitative measurement of damage, but rather to provide a visual assessment of its distribution prior to tensile testing. All image processing was conducted using LEICA LAS X software.

DETERMINING REDUCTION FACTOR FOR THE INSTALLATION DAMAGE (RFID)

All exhumed geogrid samples that exhibited uniformly damaged surfaces were tested to evaluate the reduction in tensile strength resulting from the installation damage created in this study. Tensile tests were conducted on single ribs of the geogrids following ASTM D6637 (2015)-Method B. To establish baseline tensile strength values, tensile characterization was also performed on the undamaged (virgin) geogrid samples. The reduction in tensile strength and the corresponding RFID value were determined by comparing the tensile test results of the virgin and damaged geogrid specimens. ASTM D6637 (2015) requires a minimum of six single-rib tensile tests for this evaluation. The geogrid layer retrieved from the 280 mm (11-in) diameter mold contained eight single-rib specimens, thus satisfying this requirement.

RESULTS AND DISCUSSIONS

Assessment of Installation Damage Distribution on the Geogrid Surface: To achieve uniform installation damage across the geogrid surface, a series of preliminary trials were

© ASCE

conducted by varying the top layer aggregate layer thickness (h) and compaction duration (t). Six different combinations were tested, as presented in Table 2, providing insight into the influence of each parameter on the extent and distribution of installation damage.

Table 2. Iterative experimental configurations and corresponding damage patterns

Top Layer Thickness, h mm (in)	Compaction Duration, t (minutes per location)	Damage Pattern
50.0 (2.0)	1.0	Non-uniform
	2.0	Non-uniform
	3.0	Semi-uniform
25.0 (1.0)	1.0	Semi-uniform
	2.0	Semi-uniform
	3.0	Uniform

Initial trials with a 2-inch-thick top layer and vibratory compaction durations ranging from 1 to 3 minutes per location resulted in non-uniform to semi-uniform damage patterns. In these cases, certain ribs remained largely unaffected while others exhibited localized damage. Subsequent tests with a reduced top layer thickness of 1 inch showed promising results. Even with a 1-minute compaction duration per location, a semi-uniform damage pattern was achieved as an improvement from the 2-inch condition. This outcome suggested that a thinner aggregate layer might enable more efficient energy transfer and thus more uniform damage.

As the compaction duration was progressively increased from 1 to 3 minutes per location (for 1-inch top aggregate layer), the damage distribution became increasingly uniform. Visual observations and subsequent image analysis confirmed that a 3-minute compaction duration with a 1-inch top layer consistently produced uniform installation damage across the geogrid surface (Table 2).

Figure 4 presents a specimen prepared using the configuration with an top thickness of 1 inch (25 mm) and a compaction duration of 3 minutes per location. Three corresponding images are included to illustrate the progression of damage. Figure 4a shows the virgin geogrid used as a baseline for the 3-minute compaction condition, along with a zoomed-in section highlighting the undamaged rib and junction characteristics. Figure 4b displays the geogrid subjected to installation damage. This image, accompanied by magnified views, captures the physical manifestations of damage, such as crushing, tearing, and coating detachment. Figure 4c shows the processed version of the damaged geogrid using grayscale intensity thresholding, where yellow-highlighted regions indicate the areas identified as damaged through image analysis.

RFID Values Obtained: Table 3 presents the tensile strength results, including average, maximum, minimum, and standard deviation values, obtained from 54 virgin geogrids and 24 damaged geogrids.

The average ultimate tensile strength of the virgin geogrid is found to be 1449 N, with a standard deviation of 43.0 N. This level of variability (2.9%) in the undamaged geogrid samples may be attributed to inherent differences in manufacturing tolerances, and potential minor

© ASCE

inconsistencies in the PVC coating thickness. Despite this natural variability, the virgin samples exhibited a consistent distribution of results without any outliers, indicating that the data set was representative.

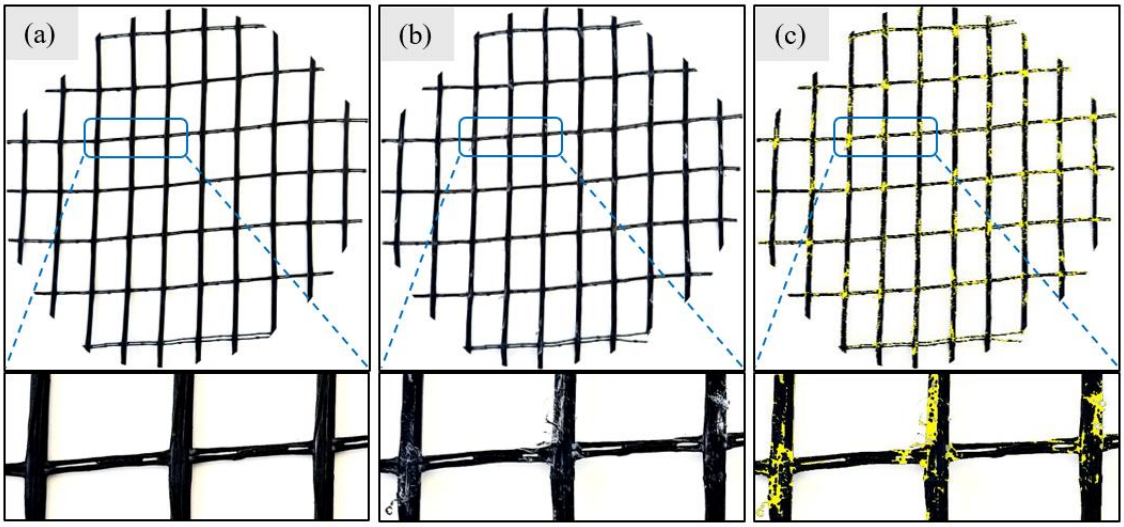


Figure 4. Assessment of installation damage uniformity on the (a) virgin geogrid, (b) damaged geogrid after compaction, and (c) image processing of damaged areas via grayscale intensity thresholding.

The average tensile strength was selected as the baseline reference value to determine the RFID. Using the mean value provides a statistically robust and repeatable basis for comparison, particularly when evaluating the performance of damaged geogrids across multiple specimens. This approach is also consistent with ASTM D6637 (2015), which recommends using the average result of a minimum of six single-rib tensile tests to represent the tensile strength of the tested geogrid.

Table 3. Summary of tensile strength test results and corresponding RFID values

	Virgin Geogrid (results from 54 tests)	h=1 in. & t=3 min. Condition (results from 24 tests)	h=1 in. & t=4 min. Condition (results from 24 tests)
Average (N)	1449	1385	1316
Maximum (N)	1552	1418	1352
Minimum (N)	1368	1345	1280
Standard Deviation (N)	43.0	21.0	22.0
RFID Obtained	-	1.046 ≈ 1.05	1.101 ≈ 1.10

As summarized in Table 3, when the geogrid specimens were subjected to 3 and 4-minute compaction durations per location, the average strengths decreased to 1385 N and 1316 N, respectively, resulting in corresponding RFID values of 1.05 and 1.10. The relatively lower standard deviations in the damaged conditions (21.0 N and 22.0 N respectively) also confirm that

© ASCE

the damage was distributed uniformly across the specimens. These results confirm that the proposed laboratory methodology in this study can reliably produce damage levels aligned with target reduction factors while maintaining consistent performance among test specimens.

CONCLUSIONS AND PRACTICAL IMPLICATIONS

Existing test methods in the literature can be used to damage geogrids; however, they do not provide guidance on how to configure the tests so that the resulting tensile strength corresponds to a specific reduction factor for installation damage (RFID). The laboratory protocol developed in this study addresses this gap by using a PVC-coated PET woven geogrid and simulating compaction-induced damage, where the damage levels correspond to target RFID values of 1.05 and 1.10. To achieve these RFID targets, the geogrid specimens were embedded between two 25 mm (1-in) aggregate layers within a 280 mm mold, and the top aggregate layer was compacted with a rotary hammer conforming to ASTM D7382 (2020). For the demonstration presented in this study with the geogrid used, uniform damage distribution was obtained at 3 minutes of compaction per location (RFID = 1.05), while increasing the duration to 4 minutes produced greater damage, corresponding to RFID = 1.10. Studies with other types of geogrids or other target RFID conditions may require different compaction durations.

The primary contribution of this study is the ability to create compaction-induced damage based on deliberately targeted RFID values, rather than creating test conditions that results in random RFID as in the case of existing standard testing protocols. The methodology presented in this study is well suited for investigations where specifically damaged geogrid specimens are needed for further investigation.

REFERENCES

Allen, T., Christopher, B., Elias, V., and DiMaggio, J. (2001). Development of the simplified method for internal stability design of mechanically stabilized earth walls (No. WA-RD 513.1,). The Department.

ASTM D5818-22. (2022). *Standard Practice for Exposure and Retrieval of Samples to Evaluate Installation Damage of Geosynthetics*. ASTM International.

ASTM D6637/D6637M-15. (2015). *Standard Test Method for Determining Tensile Properties of Geogrids by the Single of Multi-Rib Tensile Method*. ASTM International.

ASTM D7382-20. (2020). *Standard Test Methods for Determination of Maximum Dry Unit Weight of Granular Soils Using a Vibrating Hammer*. ASTM International.

BS 8006-1:2010 British Standards Institution. (2010). - *Code of practice for strengthened/reinforced soils and other fills*. BSI.

Ching-Chuan, H., and Shuay-Luen, C. (2006). Investigation of installation damage of some geogrids using laboratory tests. *Geosynthetics International*, 13(1), 23-35.

Cho, S. D., Lee, K. W., Cazzuffi, D. A., and Jeon, H. Y. (2006). Evaluation of combination effects of installation damage and creep behavior on long-term design strength of geogrids. *Polymer testing*, 25(6), 819-828.

Domiciano, M. L., Santos, E. C. G. D., and Lins da Silva, J. (2020). Geogrid mechanical damage caused by recycled construction and demolition waste (RCDW): Influence of grain size distribution. *Soils and Rocks*, 43(2), 231-246.

© ASCE

Elias, V., Christopher, B. R., Berg, R. R., and Berg, R. R. (2001). Mechanically stabilized earth walls and reinforced soil slopes: design and construction guidelines (updated version) (No. FHWA-NHI-00-043). United States. Federal Highway Administration.

El-Sherbiny, R., and Gross, B. (2009). Design service life of geogrids in mechanically stabilized earth walls. In *Proceedings of the 17th International Conference on Soil Mechanics and Geotechnical Engineering* (Volumes 1, 2, 3 and 4) (pp. 913-916). IOS Press.

Han, J., Jiang, Y., and Xu, C. (2018). Recent advances in geosynthetic-reinforced retaining walls for highway applications. *Frontiers of Structural and Civil Engineering*, 12, 239-247.

Hsieh, C. W. and Wu, J. H. (2001). Installation survivability of flexible geogrids in various pavement subgrade materials. *Transportation Research Record*, 1772, 190–196.

Huang, C. C., and Wang, Z. H. (2007). Installation damage of geogrids: influence of load intensity. *Geosynthetics International*, 14(2), 65-75.

Hufenus, R., Rüegger, R., Flum, D., and Sterba, I. J. (2005). Strength reduction factors due to installation damage of reinforcing geosynthetics. *Geotextiles and Geomembranes*, 23(5), 401-424.

ISO (International Organization for Standardization). (2019). *Geosynthetics — Index test procedure for the evaluation of mechanical damage under repeated loading — Damage caused by granular material (laboratory test method)*. (EN/ISO 10722).

Koerner, G. R., Koerner, R. M., and Elias, V. (1993). Geosynthetic installation damage under two different backfill conditions. In *Geosynthetic Soil Reinforcement Testing Procedures*. ASTM International.

Koerner, R. M. (2005). *Designing with geosynthetics* (Vol. 796). Upper Saddle River, NJ, USA: Pearson Prentice Hall.

Koerner, R. M., and Koerner, G. R. (2018). An extended data base and recommendations regarding 320 failed geosynthetic reinforced mechanically stabilized earth (MSE) walls. *Geotextiles and Geomembranes*, 46(6), 904-912.

Lim, S. Y., and McCartney, J. S. (2013). Evaluation of effect of backfill particle size on installation damage reduction factors for geogrids. *Geosynthetics International*, 20(2), 62-72.

Lopes, M. P., Recker, C., Müller-Rochholz, J., and Lopes, M. D. L. (2000). Installation damage and creep of geosynthetics and their combined effect-experimental analysis. In *Proceedings of the second European geosynthetics conference*, I-Bologna (pp. 895-897).

Powers, M. C. (1953). A new roundness scale for sedimentary particles. Journal of Sedimentary Research, 23(2), 117-119.

Shinoda, M., and Bathurst, R. J. (2004). Lateral and axial deformation of PP, HDPE, and PET geogrids under tensile load. *Geotextiles and Geomembranes*, 22(4), 205-222.

Tanyu, B. F., Sabatini, P. J., and Berg, R. R. (2008). *Earth retaining structures*. US Department.

Taylor, T. P., Collin, J. G., Boyle, S., Fishman, K., and Han, J. (2023). Design and construction of mechanically stabilized earth (MSE) walls (No. FHWA-HIF-24-002). United States. Department of Transportation. Federal Highway Administration.

Zornberg, J. G., and Christopher, B. R. (2007). *Chapter 37: geosynthetics. The Handbook of Groundwater Engineering*, 2nd Edition, Jacques W. Delleur (Editor-in-Chief), CRC Press, Taylor & Francis Group, Boca Raton, Florida, 2.

© ASCE

Comparative Study of Wicking and Conventional Geotextiles: Interface Properties and Drainage Performance for Slope Reinforcement

Jaime Suarez, S.M.ASCE[1]; Puneet Bhaskar, Ph.D., M.ASCE[2]; Darlene Goehl[3]; and Anand J. Puppala, Ph.D., D.GE, P.E., Dist.M.ASCE[4]

[1]Graduate Student, Zachry Dept. of Civil and Environmental Engineering, Texas A&M Univ., College Station, TX. Email: jd.suareza@tamu.edu
[2]Postdoctoral Associate, Texas A&M Transportation Institute, Bryan, TX. Email: p-bhaskar@tti.tamu.edu
[3]Research Engineer, Texas A&M Transportation Institute, Bryan, TX. Email: d-goehl@tti.tamu.edu
[4]A.P. and Florence Wiley Chair Professor, Zachry Dept. of Civil and Environmental Engineering, Texas A&M Univ., College Station, TX. Email: anandp@tamu.edu

ABSTRACT

Coastal infrastructure is becoming susceptible to failures due to rise in the frequency of flooding events caused by adverse weather phenomena. Water infiltration into the soil during an extreme rainfall event greatly decreases its suction, causing instability and probable collapse of geotechnical structures. The risk of potential damage to coastal highway infrastructure caused by flooding emphasizes a need for the implementation of innovative materials or methods which can rapidly and effectively drain geomaterials during and after flooding events. Wicking geotextile, made up of hydrophilic and hygroscopic fibers, is a novel geosynthetic which has been proven effective in removing moisture from pavement subgrades. While non-woven geotextiles are commonly used for drainage applications in slopes, this study evaluates and compares the performance of wicking geotextiles as reinforcement and drainage element against traditional non-woven geotextiles. Both drainage and interface properties of a wicking and non-wicking geotextile were determined using a large-scale direct shear apparatus. Tests were conducted at varying stress levels, and drainage capabilities of both geotextiles were examined using moisture sensors embedded in soil samples. The results from the tests indicate that wicking geotextile provides superior drainage and reinforcement capabilities compared to conventional non-woven geotextile.

INTRODUCTION AND BACKGROUND

Flooding constitutes a significant problem for coastal infrastructure. This threat has risen over the past decades and will continue to increase with an increase in frequency and severity of extreme weather events due to climate change (Neumann et al, 2015). There are over 60,000 miles of highways in the United States, which hold great relevance for travel, commerce, and other economic activities, at risk of coastal flooding (Douglass et al, 2014). Failures of transportation structures can cause disruption over a great area, especially in densely populated regions (Testa et al, 2015). One of the most common forms of transportation infrastructure failures is the collapse of highway embankment slopes, which is often the result of water infiltration into the soil. The effect of infiltration into the soil is softening and strength loss, which increases the probability of slope failure (Jafari & Puppala, 2018). The application of

© ASCE

adequate mitigation methods to protect coastal roadway infrastructure can save billions of dollars in potential losses (Neumann et al, 2015).

The application of geotextiles to stabilize highway embankment slopes has become a common practice, as they provide tensile resistance that counteracts the driving forces generated by the soil and other loads (Viswanadham & Mahajan, 2004). However, most geotextiles do not possess effective drainage properties. Huang (1994) reported three different geotextile-reinforced retaining walls which failed due to saturation and increased soil self-weight. Conventional geotextiles perform well in draining water from saturated soils but are largely ineffective in removing moisture from unsaturated soils when relying solely on gravity-driven drainage. (Iryo & Rowe, 2003). The flow in unsaturated soil is significantly different compared to saturated soil due to presence of matric suction (Bhaskar, 2020, Bhaskar et al, 2022). Due to the limited drainage efficiency of conventional geotextiles under unsaturated conditions, there is a growing demand for advanced materials that can improve drainage performance in geotechnical applications.

Wicking geotextile is a novel geosynthetic which can act as both a reinforcement and drainage element. This geotextile contains two types of fibers: polypropylene fibers which provide tensile strength, and additive enhanced nylon wicking fibers with grooves that provide drainage. Wicking fibers have a diameter that may vary between 30 and 50 μm, while the spacing between grooves varies between 5 and 12 μm (Lin & Zhang, 2018). Wicking geotextile has been predominantly used to drain moisture from pavements, with tests on pavement sections showing improved drainage capabilities compared to conventional geotextiles, which resulted in higher pavement stiffness and reduced deformation (Biswas et al, 2021). It has also been shown to prevent or reduce pumping (Ghalinmohadam et al, 2022) and frost heave (Lin et al, 2017). Although wicking geotextiles have shown encouraging results in pavement applications, their performance in embankment slopes—particularly in flood-prone areas—remains an area that warrants further research.

The interface strength properties of a geotextile are crucial for determining its reinforcement capabilities. These can be measured through either pullout tests or direct shear tests. However, results from these tests on the same geotextile can return slightly different values because of geotextile deformation in direct shear tests (Lopes & Silvano, 2010). The aforementioned properties depend on the geotextile and the soil used for the test. For conventional woven geotextiles, the interface friction angle may vary between 20° in clays and 30° in silts and clayey sands (Hatami & Esmaili, 2015). Esmaili et al (2014) found that reduced matric suction caused by increased moisture diminishes interface shear strength, also noting that most of the loss is represented by loss of adhesion, whereas the interface friction angle was not significantly affected. Guzman et al (2018). conducted pullout tests on geotextiles embedded in saturated soils and found that wicking geotextiles exhibited superior interface strength compared to their non-wicking counterparts. While the impact of soil moisture on geotextile-soil interface strength has been extensively studied, there is still a notable lack of research addressing how drainage behavior influences this interface strength

While the interface properties of several conventional geotextiles and a wicking geotextile have been determined separately, the results cannot be directly compared, which is necessary for an adequate decision-making process when evaluating alternatives for coastal slope protection. Therefore, the main objective of this study was to determine the soil-geotextile interface properties for a conventional and a wicking geotextile on the same soil using large-scale direct shear tests. The comparison was made based on the performance of both geotextiles after

© ASCE

flooding only and not the initial conditions. The direct shear apparatus used for the test had been previously used for the determination of soil and soil-geotextile interface properties under different saturation conditions (Bareither et al, 2008, Lin et al, 2009). Additionally, the drainage properties of both geotextiles were compared using moisture sensors installed in the soil samples used for the tests, which tracked changes in moisture over 7 days. The test results are indicative of the role played by wicking geotextiles in the preservation of interface adhesion during flooding events.

MATERIALS

Soil

Material from the area was obtained from a local supplier and a series of soil characterization tests were carried out to obtain relevant properties. Basic soil classification tests, such as sieve analysis, Atterberg limits, and standard Proctor tests, were conducted in accordance with ASTM standards, and results are tabulated in Table 1. From the results of sieve analysis test, the soil was classified as silty sand (SM-SC) with approximately 35% fine content (Figure 1(a)). A Standard Proctor test was carried out which determined its maximum dry unit weight corresponded to 20.2 kPa at 13.5% moisture content (Figure 1b). An unconfined compressive strength (UCS) test was also conducted to evaluate the strength characteristics of the soil.

Table 1. Soil properties obtained from characterization tests

Parameter	Value
Liquid Limit (%)	25
Plastic Limit (%)	15
Plasticity Index (%)	10
USCS Soil Classification	SM-SC
Unconfined Compressive Strength (kPa)	93
Maximum Dry Unit Weight (kN/m^3)	20.2

Geotextiles

Both wicking and conventional non-woven geotextiles, shown in Figures 2(a) and 2(b) respectively, were obtained from local suppliers. Their main properties, as reported by the vendors, are tabulated in Table 2.

Table 2. Geotextile properties

Parameter	Wicking GTX	Non-Woven GTX
Tensile Strength (kN/m)	77	27
Apparent Opening Size (mm)	0.425	0.3
Permittivity (sec^{-1})	0.4	2.2
Water Flow Rate (l/min/m^2)	1222	6112

© ASCE

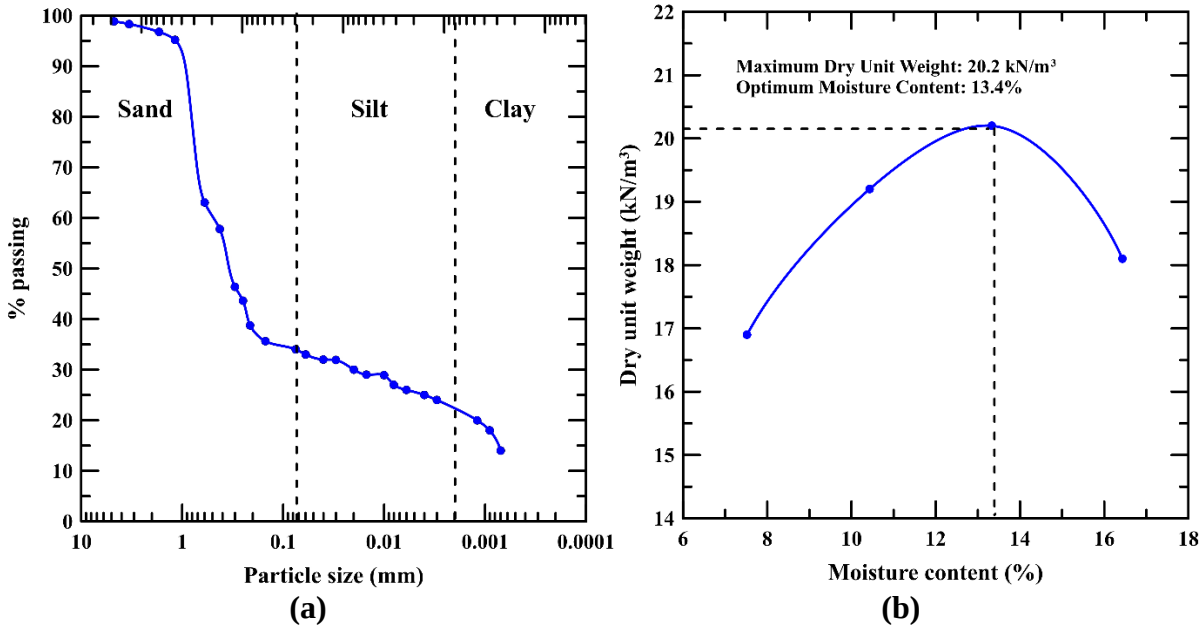


Figure 1. Soil characterization tests: (a) Grain size distribution; and (b) Proctor curve.

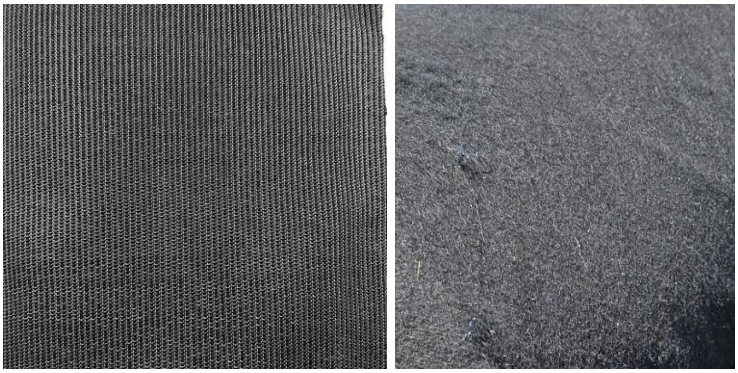


Figure 2. Geotextiles used for testing: (a) Wicking geotextile; and (b) Conventional non-woven geotextile.

TEST METHODS

Large Scale Direct Shear Box

Large-scale direct shear tests were carried out in this study to determine the interface properties of soil-non-woven geotextile, and soil-wicking geotextile interfaces. A large -scale direct shear test box, as shown in Figure 3, was used to conduct these tests. The apparatus is composed of a lower box which is 40 cm long, 30 cm wide and 10 cm in height, and a top box which is 30 cm long, 30 cm wide, and 10 cm in height. During the shearing phase of the test, the bottom box is moved horizontally by a motor while the top box is held in place by the normal stress applied through a load cell. The apparatus also allows for inundation of the soil sample and placement of sensors in the bottom box.

© ASCE



Figure 3. Large scale direct shear test setup

Testing Program and Methodology

In the experimental study, three tests at different normal stress levels were performed for both interfaces as per the method presented in ASTM D5321. For comparative performance evaluation of wicking geotextile and non-woven geotextile, the same testing conditions were kept for all tests. For the test sample preparation, oven-dried soil was mixed with the required amount of water to bring it to the target moisture content of 15.5%, which corresponds to 95% of maximum dry density on the wet side of the Proctor curve. Moist soil was then kept in a humidity control room for 24 hours in moisture equilibration and its moisture content was determined just before the sample preparation.

The moist soil was then compacted inside shear boxes in four layers using a Proctor compaction hammer. As shown in Figure 4, soil was placed and compacted in both top and bottom boxes with geotextile sandwiched between them. During the compaction of the second layer, three moisture sensors were embedded in the soil in the bottom box, approximately 2.5 cm below the interface to study drainage capabilities of soil. It should be noted that suction sensors were not used along with moisture probes because of lack of space in the shear box. After the compaction of the second layer was completed, the geotextile was clamped to the top box. The top box was then filled with soil and the remaining 2 layers of soil were compacted. The top cap was placed, and the shear box assembly was then placed in the testing device.

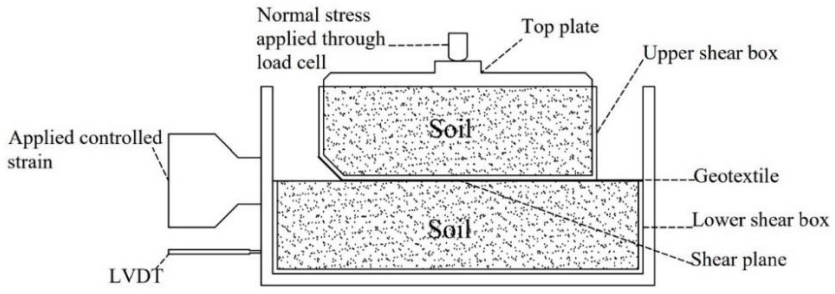


Figure 4. Schematic of large-scale direct shear box

© ASCE

Once the soil sample was prepared and placed in the apparatus, it was inundated by filling the tub of the apparatus with water up to the top level of the bottom box. The water was kept in the tub for at least 24 hours and then drained through a valve located on the bottom of the device. Simultaneously, normal stress was applied to the sample to commence the consolidation process. In the present study, tests were conducted at normal stress of 50, 100, or 200 kPa. After 24 hours of soil inundation, the sample was allowed to drain through geotextiles for 7 days. The embedded sensors recorded moisture changes in the samples every 15 minutes. Lastly, the sample was sheared under drained conditions for 24 hours at a rate of 0.03 mm/min until shear strain reached 15%, which corresponded to 46 mm of displacement.

RESULTS AND DISCUSSION

This section presents and discusses results obtained from large scale direct shear testing for both geotextiles. Interface strength parameters were calculated for soil-non-woven geotextile, and soil-wicking geotextile interface. Also, changes in soil moisture for 7 days due to drainage facilitated by geotextile after a simulated flooding event are also presented.

Throughout the tests, moisture sensors recorded the moisture variations in the soil near the interface, and results are plotted in Figure 5. The results clearly indicate that there was no significant moisture dissipation for the case of conventional non-woven geotextile, as moisture content in the soil remained mostly stationary throughout the duration of the test. In contrast, there are visible moisture variations over time for the case of the wicking geotextile, with a relatively constant rate of change throughout the testing period. This change in moisture levels is evidence of the drainage action from the wicking fibers. Furthermore, the continued drop in moisture content is indicative of the ability of wicking geotextile to drain water from soil under saturated and unsaturated conditions. While normal stress did not have a discernible impact on the rate of change in moisture content, it may have some influence on the initial moisture content, as consolidation under applied normal stress can cause moisture to be captured by the wicking geotextile, where it can then evaporate once it comes into contact with the atmosphere. Figure 5 also shows small differences in initial moisture content between the conventional and wicking geotextile. There is no trend that suggests that the choice of geotextile impacts initial moisture content. Therefore, it is considered that these small differences result from natural variations resulting from the mixing and compaction process. Higher initial water contents are associated with reduced soil adhesion. However, as the sample is subjected to shear stress after 7 days, the effect of the initial moisture content is minor compared to the influence of drainage.

Figures 6(a) and 6(b) compare the stress-displacement behavior and interface strength parameters of the soil-non-woven geotextile and soil-wicking geotextile interfaces. All samples were subjected to shearing after a 7-day drainage period facilitated by the geotextile.

The plots indicate that none of the interfaces displayed a distinct peak in shear stress. Rather, the shear strength increased sharply at the beginning, followed by a gradual and continuous rise as shearing progressed. Both geotextiles have a very similar interface friction angle, with the conventional geotextile having a slightly higher angle. However, the wicking geotextile has a significantly higher adhesion compared to its counterpart, which results in higher shear strength, especially at low normal stress values. Low value of interface adhesion in the case of the non-woven geotextile can be attributed to minimal desaturation of the soil sample for 7 days. In contrast, the drainage properties of the wicking geotextile caused higher moisture dissipation, leading to higher matric suction and the recovery of adhesion lost during the flooding event.

© ASCE

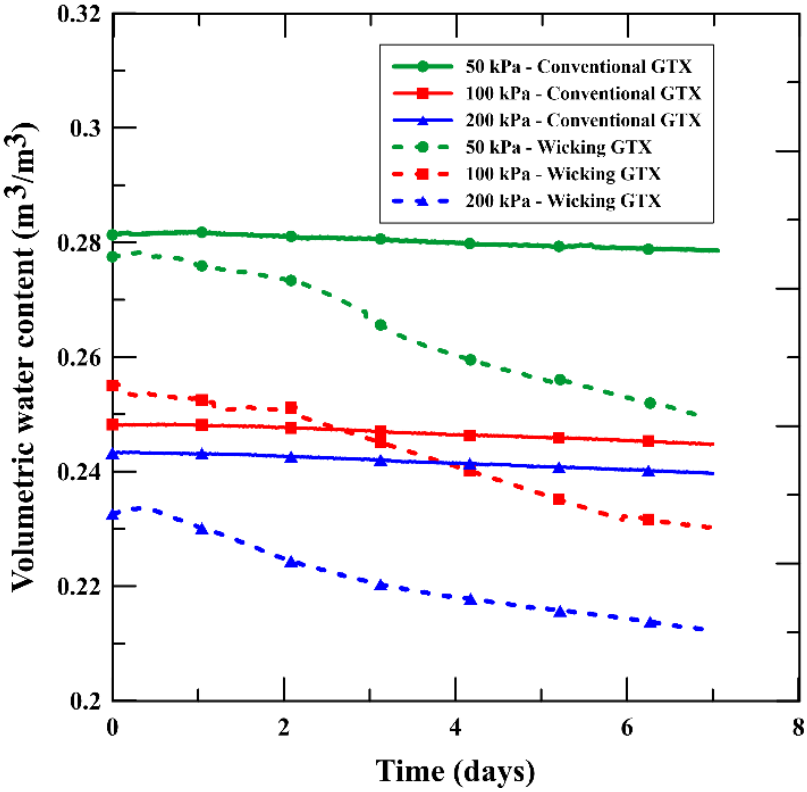


Figure 5. Moisture variation over time for conventional non-woven and wicking geotextile

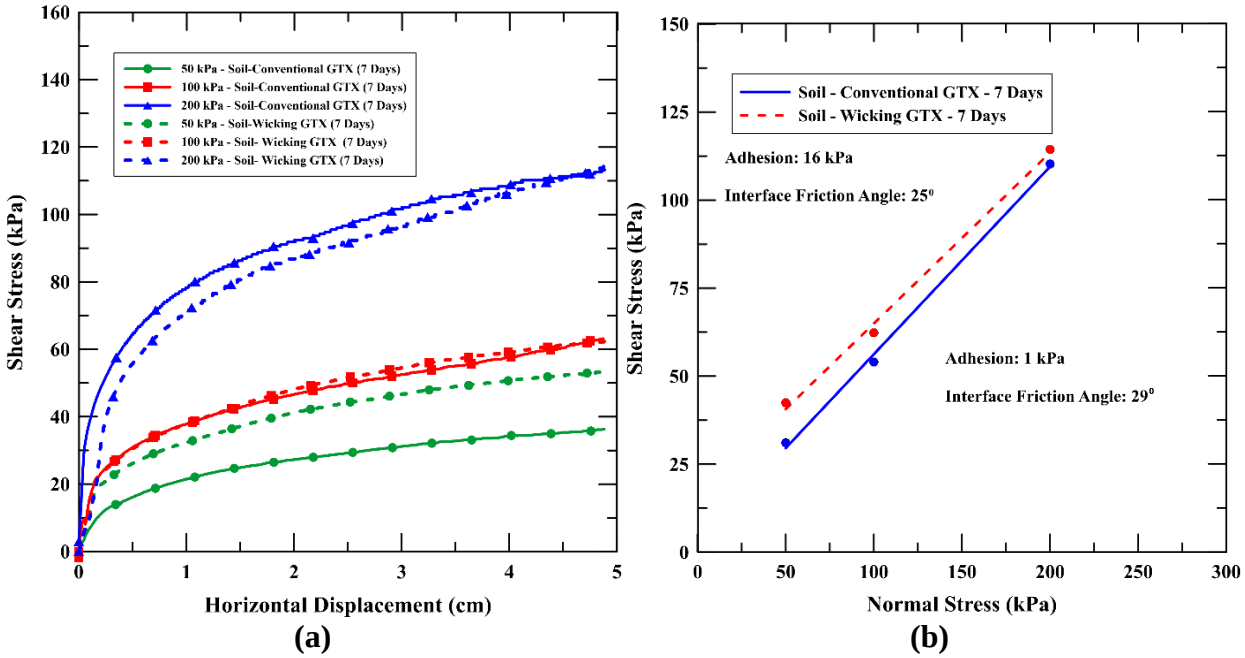


Figure 6. Interface test results for conventional non-woven and wicking geotextile: (a) Stress-displacement curves; and (b) Interface shear strength parameters.

© ASCE

At low normal stress, shear strength of a soil is governed by its cohesion, whereas strength is mostly because of frictional resistance at high normal stress. As the friction angle in both cases is almost the same, shear strength plots are similar at high normal stress values (100 kPa and 200 kPa). The difference between the two adhesion values, as presented in Table 3, can be a key predictor of the behavior of slopes and other earthen geotechnical structures reinforced with these geotextiles during wet conditions, where lack of adhesion is a critical vulnerability and can lead to failure. Despite their higher friction angle, conventional geotextiles will be ineffective in these conditions due to the total loss of adhesion. In contrast, wicking geotextiles can retain and recover adhesion quickly, therefore reducing the risk of failure. Furthermore, the slightly reduced friction angle will have little impact on the functionality of wicking geotextile, as it will only have a significant effect if there is high normal stress, which is not the case for shallow depths.

Table 3. Summary of interface properties

Strength Parameter (After 7 days)	Non-woven geotextile	Wicking geotextile
Adhesion (kPa)	1	16
Interface Friction Angle (^{o})	29	25

SUMMARY AND CONCLUSIONS

Wicking geotextile can be a promising solution and alternative to other geotextiles for providing both reinforcement and drainage in coastal embankments. As its effectiveness in pavements has been proven, this study gauges the capabilities of wicking geotextile in embankment slopes by determining its interface properties and drainage capabilities and comparing them with a conventional non-woven geotextile. To achieve this, a series of large-scale direct shear interface tests were carried out on silty sand.

The test results indicate that interface friction angle is slightly higher for conventional non-woven geotextile compared to wicking geotextile, while interface adhesion is significantly higher for wicking geotextile because of its drainage capabilities causing a reduction in soil moisture. As a result, slopes reinforced with wicking geotextile will continue to provide support to the slope during and immediately after flooding, whereas slopes with non-woven geotextiles will not benefit from any reinforcement properties and will therefore be more vulnerable to failure. Measurements from moisture sensors show there was a notable reduction in moisture content for the soil samples with wicking geotextile over 7 days, whereas the loss in moisture in the case of control soil and conventional non-woven geotextile was negligible. Compared to conventional non-woven geotextiles, wicking geotextile offers a more resilient and effective solution for infrastructure exposed to fluctuating moisture conditions, making it a valuable advancement in geosynthetic applications for coastal embankments. Future studies on this topic can aim for evaluating the effect of suction on adhesion of soil-wicking geotextile interface and its performance under different moisture conditions.

ACKNOWLEDGMENTS

The authors would like to acknowledge the support of Southern Plains Transportation Center-funded project #CY1-TTI-02.

© ASCE

REFERENCES

Bareither, C. A., Benson, C. H., and Edil, T. B. Comparison of Shear Strength of Sand Backfills Measured in Small-Scale and Large-Scale Direct Shear Tests. *Canadian Geotechnical Journal*, Vol. 45, No. 9, 2008, pp. 1224–1236. https://doi.org/10.1139/T08-058.

Bhaskar, P. *Transient Seepage and Slope Stability Analysis in Partially Saturated Earthen Dam*. University of Texas at Arlington, 2020.

Bhaskar, P., Puppala, A. J., and Boluk, B. Influence of Unsaturated Hydraulic Properties on Transient Seepage and Stability Analysis of an Earthen Dam. *International Journal of Geomechanics*, Vol. 22,No. 7, 2022, p. 04022105. https://doi.org/10.1061/(ASCE)GM.1943-5622.0002414.

Biswas, N., Puppala, A. J., Khan, M. A., Congress, S. S. C., Banerjee, A., and Chakraborty, S. (2021). Evaluating the performance of wicking geotextile in providing drainage for flexible pavements built over expansive soils. *Transportation Research Record*, 2675(9), 208-221.

Douglass, S. L., Webb, B. M., and Kilgore, R. (2014). Highways in the Coastal Environment: Assessing Extreme Events. Publication FHWA-NHI-14-006. Federal Highway Administration US Department of Transportation, Washington D.C.

Esmaili, D., Hatami, K., and Miller, G. A. (2014). Influence of matric suction on geotextile reinforcement-marginal soil interface strength. *Geotextiles and Geomembranes*, 42(2), 139-153.

Galinmoghadam, J., Liu, J., Zhang, X., Lin, C., and Guo, Y. (2022). Mitigating pumping in pavement shoulder using wicking geotextile: an experimental study. *Transportation Research Record*, 2676(11), 145-159.

Guzman, E. M. D., Kaluzny, S., and Alfaro, M. Interface Properties of Geotextiles with and without Wicking Function. 2018. *Proceedings of the 11th International Conference on Geosynthetics*.

Hatami, K., and Esmaili, D. (2015). Unsaturated soil–woven geotextile interface strength properties from small-scale pullout and interface tests. *Geosynthetics International*, 22(2), 161-172.

Huang, C. C. (1994). Report on three unsuccessful walls, In *Recent Case Histories of Permanent Geosynthetic-Reinforced Soil Retaining Walls*, Tatsuoka and Leshchinsky (eds.), Balkema, Rotterdam, 219–222.

Iryo, T., and Rowe, R. K. (2003). On the hydraulic behavior of unsaturated nonwoven geotextiles. *Geotextiles and Geomembranes*, 21(6), 381-404.

Jafari, N., and Puppala, A. J. (2018). *Prediction and rehabilitation of highway embankment slope failures in changing climate*.

Lin, C., and Zhang, X. (2018). Laboratory drainage performance of a new geotextile with wicking fabric. *Journal of Materials in Civil Engineering*, 30(11), 04018293.

Lin, C., Presler, W., Zhang, X., Jones, D., and Odgers, B. (2017). Long-term performance of wicking fabric in Alaskan pavements. *Journal of Performance of Constructed Facilities*, 31(2), D4016005.

Liu, C.-N., Ho, Y. H., and Huang, J. W. Large Scale Direct Shear Tests of Soil/PET-Yarn Geogrid Interfaces. *Geotextiles and Geomembranes*, Vol. 27, No. 1, 2009, pp. 19–30. https://doi.org/10.1016/j.geotexmem.2008.03.002.

Lopes, M. L., and Silvano, R. (2010). Soil/geotextile interface behaviour in direct shear and pullout movements. *Geotechnical and geological engineering*, 28, 791-804.

© ASCE

Neumann, J. E., Price, J., Chinowsky, P., Wright, L., Ludwig, L., Streeter, R., and Martinich, J. (2015). Climate change risks to US infrastructure: impacts on roads, bridges, coastal development, and urban drainage. *Climatic Change*, 131, 97-109.

Testa, A. C., Furtado, M. N., and Alipour, A. (2015). Resilience of coastal transportation networks faced with extreme climatic events. *Transportation Research Record*, 2532(1), 29-36.

Viswanadham, B. V. S., and Mahajan, R. (2004). Modeling of geotextile reinforced highway slopes in a geotechnical centrifuge. In *Geotechnical Engineering for Transportation Projects* (pp. 637-646).

© ASCE